

Deep Learning-based Human Detection for UAVs with Optical and Infrared Cameras: System and Experiments

Timo Hinzmänn¹

Tobias Stegemann^{1,2}

Cesar Cadena¹

Roland Siegwart¹

¹ Autonomous Systems Lab

ETH Zurich

Zurich, Switzerland

firstname.lastname@mavt.ethz.ch

² Mantis Technologies

Zurich, Switzerland

tobias@mantistechnologies.ch

Abstract

In this paper, we present our deep learning-based human detection system that uses optical (RGB) and long-wave infrared (LWIR) cameras to detect, track, localize, and re-identify humans from UAVs flying at high altitude. In each spectrum, a customized RetinaNet network with ResNet backbone provides human detections which are subsequently fused to minimize the overall false detection rate. We show that by optimizing the bounding box anchors and augmenting the image resolution the number of missed detections from high altitudes can be decreased by over 20 percent. Our proposed network is compared to different RetinaNet and YOLO variants, and to a classical optical-infrared human detection framework that uses hand-crafted features. Furthermore, along with the publication of this paper, we release a collection of annotated optical-infrared datasets recorded with different UAVs during search-and-rescue field tests and the source code of the implemented annotation tool.

1 Introduction

The need for robust human detection algorithms is tremendous and has massively increased over the past years due to the vast amount of emerging applications in the field [16, 39]. With Unmanned Aerial Vehicle (UAV) technology blooming, research in the field of human detection from aerial views also steadily evolved and experienced much interest for real-world Search and Rescue (SaR) missions [2, 4, 6, 29, 52]. While the majority of the earlier work on human detection incorporated hand-crafted features, more recent publications started to make use of Deep Learning (DL)-based detectors, mostly in the form of Convolutional Neural Networks (CNNs) [4, 15, 25]. In the superordinate field of object detection, deep CNNs have been already established for several years [28, 57], and current state-of-the-art detectors produce impressive results with possible real-time performance [33, 46]. There exist a few publications known to date that try to use these insights from the field of object detection for human detection in aerial images [8, 12, 35, 40, 62, 65]. Making use of either only optical or only Long-Wave Infrared (LWIR) (also referred to as Thermal-Infrared (TI)) images, still no work so far has considered the use of deep CNNs for combining information from both TI and optical images. As CNNs need a vast amount of data to outperform hand-crafted detectors, the lack of publicly available data might still limit the ubiquity of deep CNNs for human detection in both optical and TI aerial imagery. Available data in the field either only consists of optical [38, 50], or only TI images [14, 34, 41], and no publicly available dataset provides real-world data collected in the field for an expressive evaluation of human detection algorithms in search and rescue scenarios. Our publication

provides such a collection of optical-TI field datasets for extensive training and testing of human detection algorithms. Furthermore, besides optimizing the raw detections, we propose a complete framework to detect, track, localize, and re-identify humans, as shown in Fig. 1.

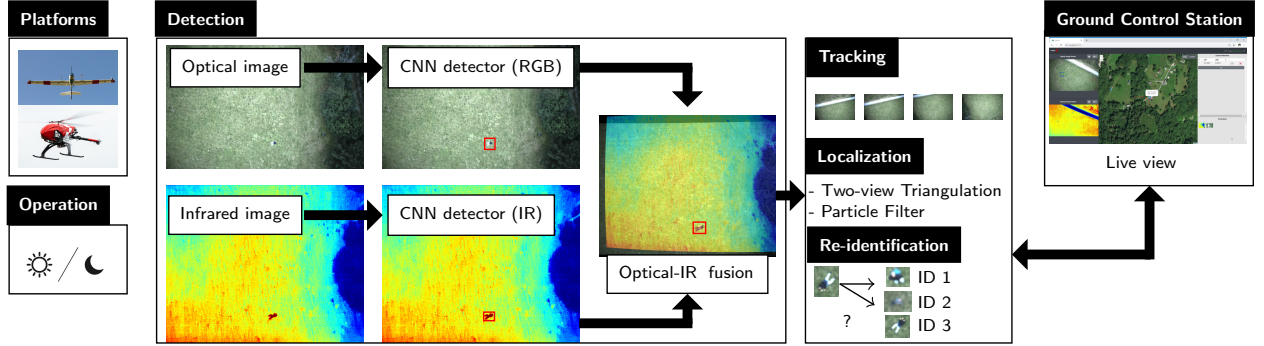


Figure 1: Proposed deep learning-based human detection system that uses optical (RGB) and long-wave infrared (LWIR) cameras to detect, track, localize, and re-identify humans from UAVs flying at high altitudes.

2 Related Work

Early work in the field of human detection from UAVs [6, 19, 20, 29, 52, 59] strongly resembled the one from object detection and applied classical methods such as Haar-like features introduced by [61], the Felzenszwalb detector [17], or Histogram of Oriented Gradient (HOG) features together with linear Support Vector Machine (SVM) classifiers as introduced by [13]. A lot of this early work [7, 19, 20, 29, 52] concluded that the combination of TI and optical images is highly beneficial for the task of human detection from high aerial views.

With the rise of deep learning, the application of CNNs started to become well-established for the task of human detection from aerial views [4, 15, 25, 55]. By comparing against more classical feature extractors and detectors such as Haar, HOG or SVM, an improvement in detection performance as well as a better generalization when using CNNs, was stated throughout. Research in object detection progressed quickly and gradually yielded deeper, better, and faster-performing object detection networks. On the side of two-stage detectors, the R-CNN network and its successors [21, 22, 49], as well as Feature Pyramid Networks (FPNs) by [32] gained a lot of attention. On the other hand, first one-stage detectors such as YOLO and its successors [45–47] or the Single Shot Detector (SSD) by [36], impressed with high frame-rates while still achieving competitive detection performance. Some recent work in the field already started to include these state-of-the-art object detectors such as adaptations of the R-CNN network [35, 40] or one-stage detectors such as YOLO9000 or SSD [12, 65] into their pipelines. The use of either one-stage or two-stage object detectors, however, results in a speed-accuracy trade-off, as shown by [8]. This is in accordance with recent findings by [33]. Their one-stage object detector framework called RetinaNet tries to address this discrepancy between inference speed and detection performance and close the gap between state-of-the-art one-stage and two-stage object detection frameworks. Wang et al. [62], for instance, used RetinaNet [33] as a proposed solution for object detection in aerial views. RetinaNet was evaluated against other one-stage and two-stage detectors, namely SSD and Faster R-CNN on the Stanford drone dataset [50]. The evaluation resulted in a similar statement to the one by [33], showing state-of-the-art performance of RetinaNet compared to two-stage detectors, while running at speeds comparable to the ones obtained from one-stage detectors. This motivates the use of these state-of-the-art one stage detectors also for our task, since their fast inference speeds are crucial when running on-board a UAV with limited computing power.

The vast majority of deep learning architectures is trained and evaluated on optical imagery. In fact, to the

best of our knowledge, the only work to date which uses a DL-based human detector on thermal imagery from a UAV was conducted by [8] in 2018, where a Faster R-CNN framework was applied to detect poachers in thermal images. More so, none of the publications make use of *both* the optical and thermal domain together with recent state-of-the-art deep object detection networks. Likely, this is due to the lack of publicly available data: Publicly available datasets either only consist of optical images [38, 50] or only thermal images [14, 34, 41]. In this paper, we approach these research gaps as follows: Firstly, we present a comprehensive performance comparison of state-of-the-art human detection architectures, trained with optical and thermal imagery. In particular, the evaluation comprises YOLO and RetinaNet with different ResNet backbones. For reference, we additionally provide the results from a hand-crafted thermal-optical human detection pipeline [29]. Secondly, to the best of our knowledge, this paper constitutes the first publication on deep learning-based human detection from UAVs which combines optical-thermal imagery. The employed merging strategy is explained in detail in Sec. 3.3. Thirdly, the evaluation is conducted on datasets recorded during SaR field tests. The collection of annotated datasets and the implemented annotation tool is released along with this paper. Despite the great success of recent findings in the field of object detection, very small sample sizes as well as strong-view point variations in aerial images, make the task challenging. Recent work like the one by [35] or [12], clearly shows that adaptations to current object detection networks are crucial for a decent performance on aerial images from UAVs. In this paper, we propose to use optimized custom anchors and up-scaled images to boost the detection from high altitudes and reveal this performance gain in a detailed evaluation. Finally, we describe in detail our approach to track, localize, and re-identify humans to improve the overall performance beyond the raw detection.

3 Human Detection

3.1 State-of-the-Art Object Detectors Revisited

Our proposed pipeline uses a customized RetinaNet network with a ResNet50 backbone as introduced by [33] as a state-of-the-art one-stage object detector. As already outlined, this is mainly due to limited computing resources on-board of UAVs, as well as similar detection performance of RetinaNet compared to two-stage detectors in recent publications [33, 62]. Our implementation follows the original implementation and introduces crucial customizations, as outlined in Sec 3.2. This proposed framework is then compared against YOLOv3 using a darknet-53 backbone, another state of the art one-stage object detector. Both networks follow a similar basic architecture collecting features at different scales using their respective backbone networks and subsequently regressing and classifying the output bounding boxes. As one of their main contributions, RetinaNet introduces a novel focal loss, based on the well-known cross-entropy loss. Since YOLOv3 still relies on the standard cross-entropy loss, the focal loss further constitutes the main difference between these two object detection frameworks. In [33], Lin et al. state the significant imbalance of image background and foreground in many object detection tasks as the main reason for lacking the performance of conventional one-stage detectors. They were able to show that a conventional cross-entropy loss is easily overwhelmed by the vast amount of background samples seen during training, when running regression and classification directly on top of a dense feature map. By adding a modulating factor $(1 - p_t)^\gamma$ to the cross-entropy loss, they define the novel focal loss using a tunable focusing parameter $\gamma > 0$, able to counteract this large imbalance.

3.2 Network Customization

3.2.1 Optimal Anchor Selection

Both RetinaNet as well as YOLOv3 use nine anchor bounding boxes for final bounding box regression. While RetinaNet uses fixed hand-picked anchors, YOLOv3 uses k-means dimension clustering on the COCO dataset [31] to find optimal anchors. Furthermore, during training, the selection strategies, deciding on which anchor bounding boxes are assigned to the ground-truth bounding boxes, differ quite significantly

between the two networks. Lin et al. [33] use an adjusted assignment rule originating the region proposal network of Faster R-CNN [49]. Anchors are assigned to ground-truth boxes for an Intersection over Union (IoU) value of 0.5 or higher and to background for IoU values in $[0, 0.4)$. Each anchor is assigned to at most one ground-truth box, and all remaining unassigned anchors are ignored during training. Redmon et al. [46], on the other hand, do not use such a dual IoU threshold. Instead, they simply assign one anchor per ground-truth bounding box by using the anchor with the largest IoU value. If an anchor is not the best but overlaps a ground-truth box with more than 0.5 IoU, the prediction is ignored. All other anchors, not assigned to any ground-truth boxes, do only incur a loss for the object prediction. The need for customized anchors in our pipeline is crucial: Using the standard anchors for RetinaNet on our training dataset showed that a lot of samples in both optical and thermal images did not contribute to the training process because of their really small size and not reaching an IoU value of 0.4 or higher with any of the standard anchor bounding boxes. Resolving this by changing the added anchor sizes at each level of the original publication by [33] to custom sizes of $\{2^{-2}, 2^{-1}, 2^0\}$, the number of bounding boxes contributing to the training was sufficiently increased. More specifically, the amount of optical samples contributing to the final stage of training was increased from 57.7% to 97% on the optical side and from 33.2% to 88.1% on the thermal side of our training dataset.

3.2.2 Image Resolution Augmentation

A second natural way of improving the detection of really small bounding boxes is to simply augment their sizes. Final detection performance can be improved significantly, by either using augmented- or higher-resolution images, as also stated by Bejiga et al. [4]. This can be achieved by increasing the input image size during inference since both networks being fully-convolutional. Doubling the standard image sizes of the RetinaNet variants was able to bring a considerable performance improvement as shown in Sec. 6.

3.3 Optical-Infrared Merging Strategy

The proposed pipeline utilizes optical and thermal imagery. This is especially useful to further reduce false positives during day flights, for detecting humans during night flights, or to find humans in aggravated optical conditions, for instance, when obscured by shadows due to large rocks or trees. The camera intrinsic and extrinsic parameters are used to map feature positions from the optical to the thermal image and vice versa. However, small inaccuracies in the calibration, the image triggering, or exposure time may result in pixel offsets in both spectra. Especially in applications with fast-moving and fast-turning UAVs this may become an issue. To account for these inaccuracies, we propose to use a sliding window to match bounding boxes between the spectra, as illustrated in Fig. 2. More specifically, a rectangle nine times the size of the mapped bounding box is searched for a target bounding box using 36 sliding window steps in total. Matching of the sliding window and target bounding boxes is done similarly to the standard procedure proposed by [16], using an IoU threshold of 0.5. After a completed matching step, a logical OR merging scenario is used, considering all bounding boxes from both domains while averaging the respective prediction scores.

3.4 Network Training

To train the network, publicly available, external datasets, as well as internal data, recorded by one of our UAVs, are used. Using the implemented annotation tool, a total of 11 optical sequences consisting of 40 445 images, and 14 thermal sequences containing 1029 images are available for training. The human bounding boxes in these sequences are annotated with a distinct ID for each individual human, attributes for the pose (upright, sitting or lying), and an occlusion attribute. Altogether, the newly collected datasets add up to a total of 34 022 human bounding boxes in the optical images, and 37 228 human bounding boxes in the thermal images. In addition to our internal datasets, all available public datasets containing humans from both optical [9, 38, 50] and thermal [14, 27, 34, 41, 63] aerial views have been gathered. Together with these external datasets, the final amount of available data at hand consisted of around 1 000 000 annotations in over 170 000 optical images, and around 200 000 annotations in over 100 000 thermal images.

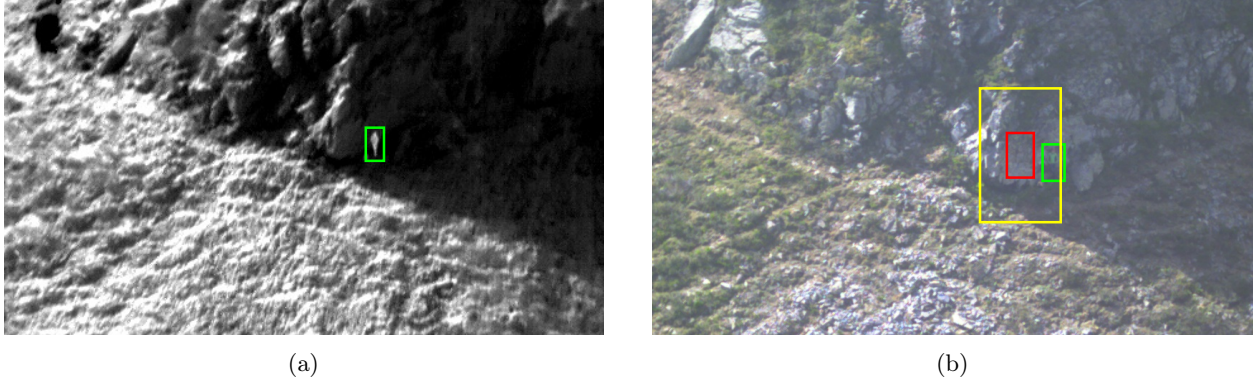


Figure 2: Exemplary matching process. Original detection in the thermal image on the left in green. Raw mapped bounding box in the right optical image in red, sliding window area in yellow and final matched bounding box (detection) in green.

The final training of the two object detectors was conducted using a two-stage training procedure: Starting with pre-trained Imagenet [53] weights, an initial pre-training step was carried out using all the data at hand, including our newly collected dataset and all available external datasets. The best results in pre-training were achieved by freezing all the backbone weights for both RetinaNet and YOLOv3 and only training and adapting all other, randomly initialized weights to the novel domain. Subsequently, the resulting weights of the pre-training step were then used to initialize a final fine-tuning step. In this step, only the newly collected, domain-specific data was used to train all the layers of both the networks. Training of the two object detectors was carried out according to the original publications of RetinaNet [33] and YOLOv3 [46]. Both networks were trained on a cluster using Nvidia GeForce GTX 1080 Ti GPUs. While YOLOv3 originally uses a smaller sized input image together with a multi-scale training strategy [46], RetinaNet uses a larger single size input image during training. To be able to train both networks using a similar batch size of eight images, RetinaNet was trained on a total of eight GPUs while YOLOv3 was trainable on a single GPU. Both networks include data augmentation and other training features mentioned in the original publications. Randomly selected sequences out of the external datasets were used as validation sets in pre-training and a fixed sequence of our own dataset was used as validation set for the final fine-tuning training scenario.

4 Human Localization and Re-Detection

This section describes our approach to track, localize, and re-detect humans in the optical spectrum based on qualitative results.

Human Tracking: For every observation classified as human the detector described in Sec. 3 creates a new victim ID. However, the final goal of the proposed framework is to associate every victim with a unique ID and to compute its position or path in 3D. In a first step towards this goal, an object tracker bundles all detections of a victim as long as the human is within the field of view of the camera (cf. Fig. 3). The human tracking is tested on the optical image stream with a frame-rate of 4 Hz, resulting in potentially large pixel displacements of an observation between two subsequent frames. To reduce the pixel displacement and simultaneously increase the speed of the tracker the image is half-sampled. Object trackers implemented in [11] were tested, including MIL [3], KCF [24], GOTURN [23], among which CSRT [37] performed best and was selected.

Human Localization: Given a track of observations in the form of bounding boxes and the corresponding camera poses, the 3D path of the object can be estimated. The camera poses are assumed to be given as

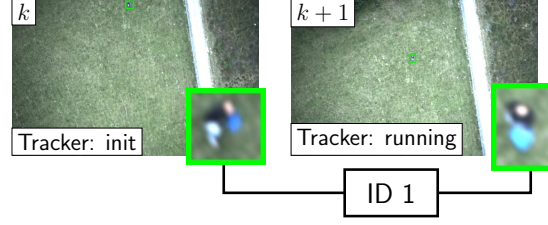


Figure 3: Human tracking: Humans that are tracked across subsequent frames ($k, k + 1$) are assigned the same human ID.

input to the framework. As the human may be non-static, two-view triangulation of consecutive observations are used. The center of the bounding box is selected for triangulation, as illustrated in Fig. 4.

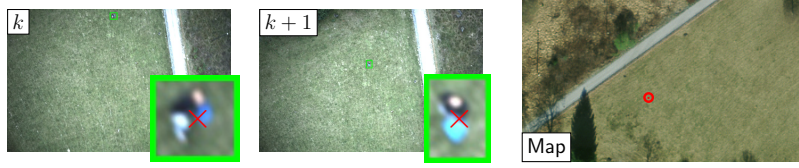


Figure 4: Human localization: Based on two subsequent detections, the geo-referenced human position can be triangulated, as visualized in the satellite orthoimage.

Metric Outlier Rejection: The metric bounding box area is used to reject false detections as follows: Given two consecutive observations of an object and the triangulated 3D object position \mathbf{p}_h^W , the depth d can be inferred via $d = \|\mathbf{p}_{\text{UAV}}^W - \mathbf{p}_h^W\|_2$. The depth is then used to transfer the bounding box from pixel coordinates to meters, resulting in the points $\mathbf{p}_i^W, i = (1, \dots, 4)$ (clockwise). The metric area of the bounding box is then $A = 0.5(\mathbf{p}_1^W \mathbf{p}_2^W \times \mathbf{p}_1^W \mathbf{p}_3^W + \mathbf{p}_1^W \mathbf{p}_3^W \times \mathbf{p}_1^W \mathbf{p}_4^W)$. Objects with bounding box areas $A > T_{\text{area}}$ are classified as outliers and rejected as visualized in Fig. 5.

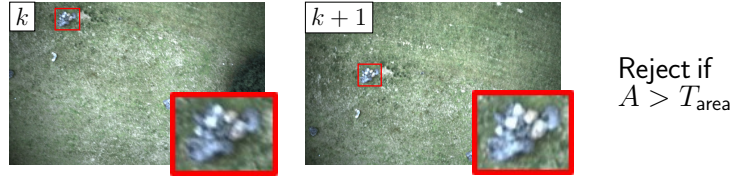


Figure 5: Metric outlier rejection: The detection is rejected if the estimated metric area A of the bounding box is above a threshold T_{area} .

Particle Filter: To handle occlusions, re-detections, and to incorporate a probabilistic motion model, a Particle Filter (PF) is initialized for every human. For computational reasons the PF is restricted to two dimensions x and y in Universal Transverse Mercator (UTM) coordinates. If necessary, the altitude of the victim can be queried from the existing map. The PF implementation and notation closely follows [56] (cf. Fig. 6):

- **Initialization:** Given the first triangulated position, denoted as $\mathbf{z}_0 = (x, y)$ with $\sigma_{\mathbf{z}} = 3$, randomly draw $N = 100$ initial particles $\mathbf{x}_{0,i}^+$ with $i = \{1, \dots, N\}$ from $\mathcal{N} \sim (\mu = \mathbf{z}_0, \sigma = \sigma_{\mathbf{z}})$.
- **Propagation:** In the propagation step, compute the a priori particles $\mathbf{x}_{k,i}^-$ given a random walk motion model, assuming a maximum human velocity $\mathbf{v}_{\text{max}} = 1.2 \frac{\text{m}}{\text{s}}$ in both, the x - and y -direction:

$\mathbf{x}_{k,i}^- = f_{k-1}(\mathbf{x}_{k-1,i}^+, \mathbf{w}_{k-1}^i) = \mathbf{x}_{k-1,i}^+ + \mathbf{w}_{k-1}^i \Delta t$ where \mathbf{w}_{k-1}^i is a random velocity \mathbf{v}_{rand} drawn from the uniform distribution $\mathcal{U} \sim (-v_{\text{max}}, v_{\text{max}})$ and Δt is the time difference between two consecutive frames in seconds.

- **Measurement:** Given a new observation \mathbf{z}_k associated with the victim ID, compute the relative likelihood q_i of this observation for every particle $\mathbf{x}_{k,i}^-$ by evaluating the conditional Probability Density Function (PDF) $p(\mathbf{z}_k | \mathbf{x}_{k,i}^-)$ based on the measurement equation:

$q_i \sim \alpha^{-1} \exp(-0.5(\mathbf{z}_k - \mathbf{x}_{k,i}^-)^\top \mathbf{R}^{-1}(\mathbf{z}_k - \mathbf{x}_{k,i}^-))$ with $\alpha = 2\pi \det(\mathbf{R})^{\frac{1}{2}}$ and measurement noise $\mathbf{R} = \sigma_z \cdot \mathbf{I}_{2 \times 2}$. Normalize via $q_i = \beta^{-1} q_i$ with $\beta = \sum_{j=1}^N q_j$.

- **Resampling:** Draw posteriori particles $\mathbf{x}_{k,i}^+$ based on normalized likelihoods q_i using Systematic Resampling (SR) [26].

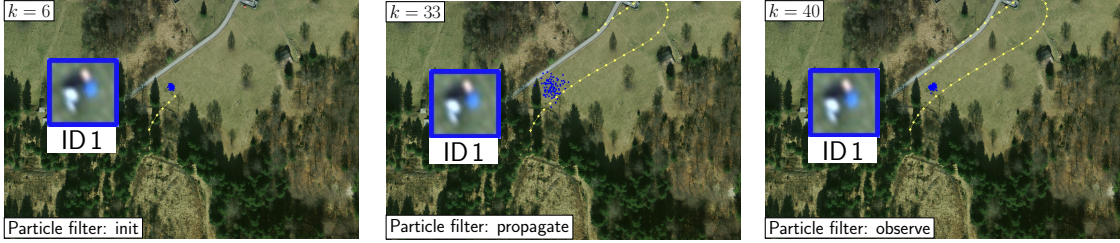


Figure 6: Particle filter: The particles for human ID 1 are visualized as blue points, the trajectory flown by the Rega drone is shown in yellow.

Human re-detection: If the UAV flies over a previously visited area and the detector returns an object classified as human, the algorithm needs to decide if the new detection z can be associated to an already observed human h_i or if it is, in fact, a new victim (cf. Fig. 7).

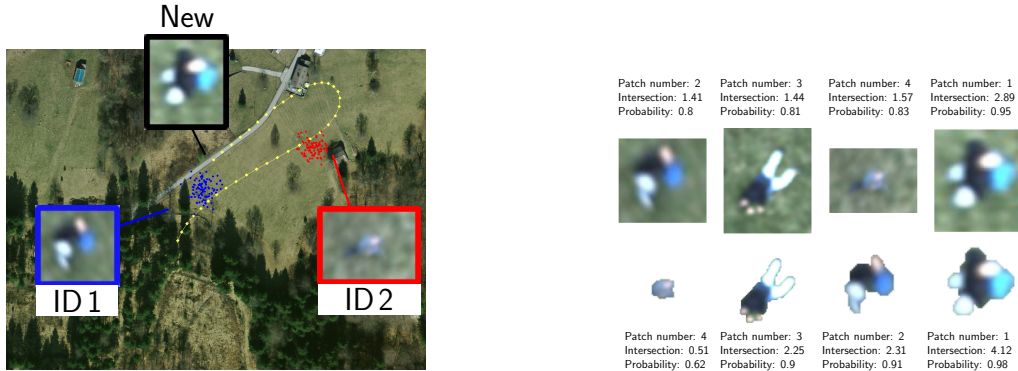


Figure 7: Human re-detection: The algorithm needs to decide if the new detection can be associated to an already observed human or if it is, in fact, a new victim. On the right, the histogram similarity is evaluated based on the Intersection metric. The query image is patch number 1.

Applying the Bayes theorem the probability $p(h_i | z)$ that the new observation z belongs to human h_i can be computed with $p(h_i | z) = \gamma^{-1} p(z | h_i) p(h_i)$, $\gamma = \sum p(z | h_i) p(h_i)$. Appearance-based and spatial information are used to compute $p(h_i | z)$. Firstly, the conditional probability $p(z | h_i)$ is computed based on the triangulated location of the new observation and all existing humans currently tracked by PFs. If $p(z | h_i) p(h_i) < T_{\text{redetect}} \forall i$ a new victim with corresponding PF is initialized. Otherwise the new detection is associated with $\arg \max_{h_i} p(h_i | z)$, i.e., with that human that maximizes the detection probability.

Secondly, the prior $p(h_i)$ which is the probability of observing human h_i is inferred from the similarity between a patch from human h_i and the newly detected human patch using a binary classifier. Since the

humans are detected from a high distance we base our decision if two patches contain the same person solely on the color information. Tab. 1 presents the similarity between patches computed by comparing their color histograms using the metrics [10] Correlation, Chi-square, Intersection, and Bhattacharyya [5]. The patch numbers 1 to 4 correspond to the detections shown in Fig. 7. Note that for Correlation and Intersection, higher values correspond to a higher similarity. In contrast, for the metric Chi-square and Bhattacharyya, the lower the value, the higher the similarity. Patch numbers 1, 2, and 3 are observations of the same human. However, this is not reflected by the results in Tab. 1 as the background has an influence on the color histogram. Therefore, using the GrabCut algorithm [51], the background is automatically subtracted (cf. Fig. 7) before computing the histogram which improves the re-identification results, as shown in Tab. 2. Using the sigmoid function, for instance, the results from the Intersection metric are mapped to values between 0 and 1, as shown in Fig. 7.

Method	Patch			
	1	2	3	4
Correlation	1.0	0.71	0.83	0.83
Chi-Square	0.0	8.85	2.39	2.52
Intersection	2.89	1.41	1.44	1.57
Bhattacharyya	0.0	0.53	0.37	0.44

Table 1: Quantitative results for Fig. 7: Patch similarity **without** background subtraction and histogram comparison.

Method	Patch			
	1	2	3	4
Correlation	1.0	0.57	0.83	0.09
Chi-Square	0.0	12.33	1.9	44.92
Intersection	4.12	2.31	2.25	0.51
Bhattacharyya	0.0	0.52	0.41	0.83

Table 2: Quantitative results for Fig. 7: Patch similarity **with** background subtraction and histogram comparison.

5 Hardware & Experiment Preparation

5.1 Platform and Sensors

The sensorpod used for our experiments is shown in Fig. 8c. It consists of an IDS UI-5261SE-C-HQ-R4 1.92 MP RGB camera with a C-mount lens and a horizontal field of view of 32° and an infrared camera FLIR Tau2 with a resolution of 640×480 pixel. The FLIR Tau2 is mounted on a Teax image grabber with USB2 interface. The GPU is a Jetson TX2 mounted on an Auvideo J120 carrier board and is used for network inference at run-time. It is connected to the CPU, an UP² board with Intel Atom Processor, via Ethernet. The CPU has a MSATA storage of 1 TB and handles the triggering of RGB camera, infrared camera, and ADIS16448 Inertial Measurement Unit (IMU). The casing features a plexiglass and Germanium window for the optical and infrared camera, respectively, and a fan for additional air circulation. The two UAV platforms that are used for the various test flights are shown in Fig. 8a and 8b.

5.2 Geometric Optical-Infrared Camera and Camera-IMU Calibration

The camera intrinsics (focal length, principal point), distortion parameters, and optical-infrared extrinsics (relative pose between the cameras and IMU) are required for optical-infrared image fusion and metric human localization. For this purpose, different optical-infrared, i.e., dual-modal calibration targets have been developed and improved over time. A dual-modal calibration target allows to directly calibrate the relative pose between the thermal and optical camera without the need for a camera-IMU calibration as an intermediate step. That is the optical-infrared camera can be calibrated as a stereo rig with one single calibration dataset using Kalibr [48]. The evolution of our developed calibration targets is represented by Tab. 3 and was inspired by the related publications listed in Tab. 4. The different calibration targets shown in Tab. 3 and 4 are classified based on the taxonomy proposed in [44]: Initial works utilized classical optical checkerboard calibration targets and heated the target with a flood lamp (cf. target No.1 or [42]). Based on the emissivity difference of black and white squares, the pattern can be made visible also in the TI spectrum. However, fuzzy transitions between black and white edges lead to missed or inaccurate corner detections and

unsatisfying calibration results. Based on this finding, we attempted to increase the sharpness of the edges by using materials with contrary emissivity properties. For this we designed target No.2 which is made out of black colored wood (emissivity ≈ 0.8 [30]) and aluminum (emissivity ≈ 0.095 [30]). Likewise, the authors of [54, 58, 60] focused on improving the contrast of checkerboard targets using different materials and masks. However, as for instance pointed out by [64], the corner detection remains inherently error-prone in the TI spectrum, and instead, the usage of circular features is advised. Our final dual-modal calibration target No.3 consists of 6×7 circular features, laser-cut into an aluminum calibration target, and filled with machine-cut black wooden plates. Based on the detections, the camera intrinsics and extrinsics are calibrated with

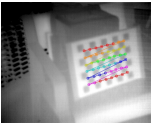

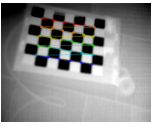
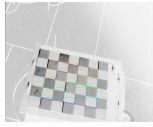
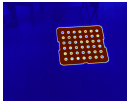

	Picture IR	Picture RGB	RGB	IR	Target type	Working Principle	Features
No.1			✓	✓	Checkerboard Paper print-out glued on wood	Color emissivity difference (black, white)	Corners 6×8 squares 0.036 m
No.2			✓	✓	Checkerboard Black colored wooden squares, Aluminum squares	Color emissivity difference (black, white) Material emissivity difference (wood, aluminum)	Corners 5×6 squares 0.036 m
No.3			✓	✓	Square grid Aluminum target with inserted black wooden circles	Color emissivity difference (black, white) Material emissivity difference (wood, aluminum)	Circles 7×6 circles 0.08 m

Table 3: Evolution of our dual-modal calibration targets (sorted by date).

Kalibr [48]. To be able to use Kalibr, the infrared images are inverted and thresholded. We obtained the best calibration results for datasets that are recorded outside where the calibration target is facing the clear sky. For this target, Kalibr reports the following errors: For a single camera calibration $\sigma = 0.09$ (infrared) and $\sigma = 0.09$ (optical); for a camera-IMU calibration $e_{\text{reproj}} = 0.60$ (infrared) and $e_{\text{reproj}} = 0.25$ (optical).

5.3 Optical-Infrared Dataset Collection and Annotation

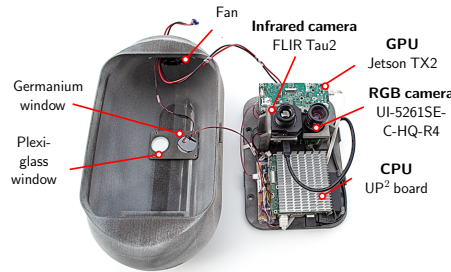
To further increase the amount of training, validation, and test data we collected additional optical-infrared datasets. The datasets are recorded with sensors mounted on the platforms listed in Fig. 8a and 8b, at



(a) Techpod



(b) Rega drone



(c) Sensorpod with optical-infrared stereo rig.

Figure 8: The sensorpod with optical-infrared stereo rig carried by the Rega drone.

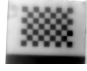





Publication	Picture	RGB	IR	Target type	Working Principle	Features
[42]		✓ ^a	✓	Checkerboard	Flood lamp Color emissivity difference (black, white)	Corners
[58]		✓	✓	Hermann grid	Material emissivity difference (Styrofoam, air)	Corners
[60]		✓	✓	Hermann grid	Heated backdrop, e.g. monitor Material emissivity difference (cardboard, monitor) difference in temperature and/or difference in thermal emissivity	Corners
[64]		✓	✓	Cross	Difference in temperature (Thermostatic heaters) Color emissivity difference (black, white)	Circles
[54]		✓	✓	Checkerboard	Flood light Color emissivity difference (black, white) Material emissivity difference (ceramic, paper)	Corners
[18]		✓	✓	Wall	Temperature difference (flood lights, fan) Color emissivity difference (black, white) Material emissivity difference (foam, aluminum)	Arcs

Table 4: Optical and infrared calibration methods (sorted by publication date)

^aNot shown in the paper but in principle possible

different locations and resembling realistic search-and-rescue missions. A complete list of available datasets is shown in Tab. 5. Along with all datasets we release the C++ based annotation tool that takes as input a dataset in the form of a rosbag [43] or video. With the help of this tool, all humans appearing in the collected data have been annotated using upright rectangular bounding boxes. During the labeling process, humans are assigned a unique ID. Every annotation contains an additional attribute for the human posture (*upright*, *sitting* or *lying*) and one for occlusion (*occluded*, *not occluded*). Examples of the available annotated frames are illustrated in Fig. 15.

6 Experiments and Results

6.1 Experiment 1: Comparison of RetinaNet, YOLOv3 and Hand-crafted Detector

In a first step, we compare the vanilla deep learning-based detectors to a hand-crafted human detection framework that uses HOG features together with a SVM classifier [29] and that serves as a low baseline solution. This reference pipeline, that was introduced in [29], detects humans in thermal imagery and then uses the corresponding optical image solely to reduce false positives. The performance on the collected **roof_test** dataset, similar to the one by [29], is illustrated in Fig. 9 and 10, and shows a significant improvement when using deep learning-based object detectors. Furthermore, all of the RetinaNet variants vastly outperform the YOLOv3 framework.

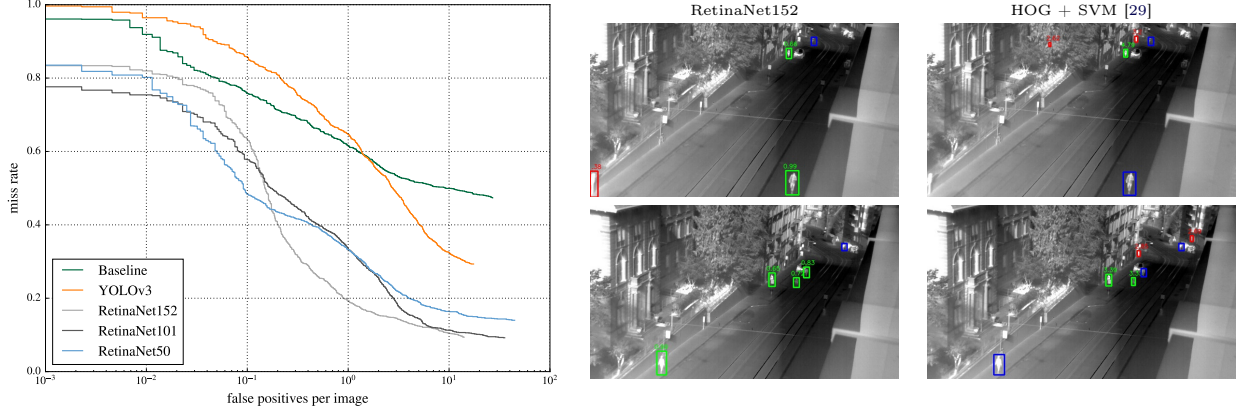


Figure 9: Thermal fppi/missrate curves on the `roof_test` set illustrating the large performance improve of deep learning detectors.

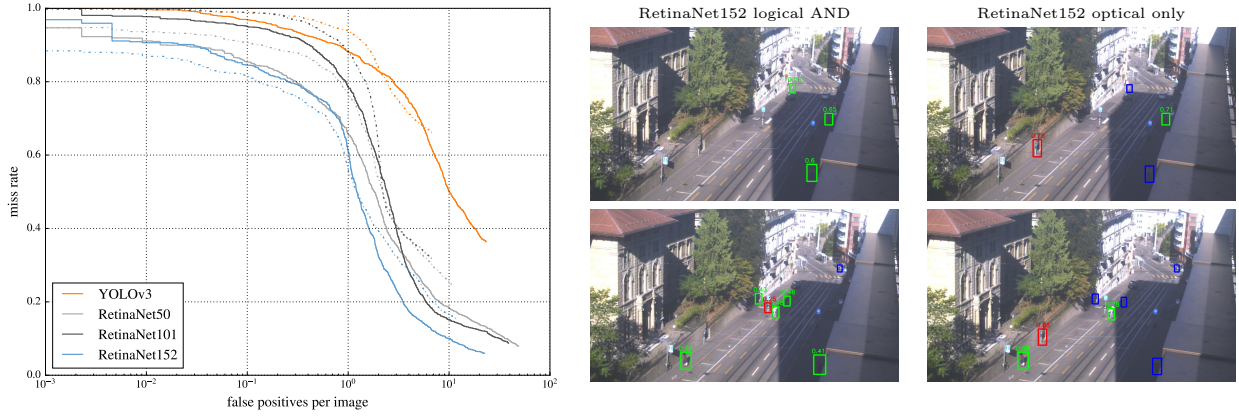


Figure 10: Optical fppi/missrate curves on the `roof_test` set. Performance on pure optical information plotted as dashed lines and the improved performance using the logical OR merging scenario in bold. By combining optical and thermal information, both false positives and overall missrates are reduced.

6.2 Experiment 2: RetinaNet evaluation in SaR scenario

In this section, the performance of the proposed human detection pipeline is thoroughly evaluated based on a dataset resembling a search-and-rescue scenario. The `field_test` datasets proved to be very challenging with a lot of very small human samples at different poses recorded from very high aerial views. Occasional motion-blur due to the flight maneuvers and a lot of heated up rocks make the thermal imagery even more challenging. The performance of our vanilla detectors on the total optical and thermal field evaluation datasets clearly emphasizes this: Only a few percents of the total amount of human bounding boxes are detected. Still, RetinaNet variants and especially the proposed RetinaNet50 network vastly outperforms YOLOv3 in the number of total detectable humans, as depicted in Fig. 11. Finally, modifications to the best performing RetinaNet50 variant, as described in Sec. 3.2, show vast improvements for the `field_test` dataset as illustrated in Fig. 12. While the logical OR merging scenario of optical and thermal detections already brings a performance improvement, the customized anchor bounding boxes vastly increase detection performance and boost up the total amount of detectable bounding boxes by over 7%. Finally, doubling the image size during inference further increases this amount to a total of 70% detected bounding boxes while making less than one false positive per image. This is an improvement of over 20% when compared to the plain version of the original RetinaNet50 variant.

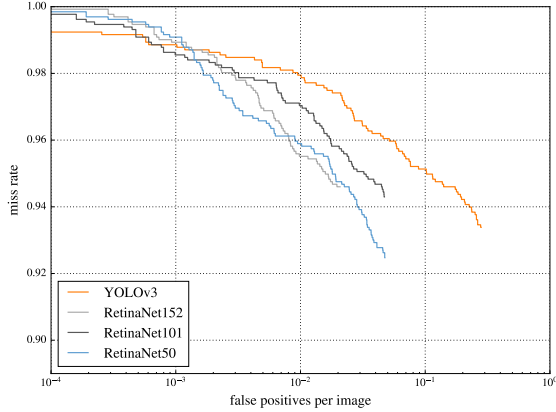


Figure 11: Performance of all networks on the total **field_test** sets using standard networks without any changes on anchors, image resolution or any merging of IR-RGB information.

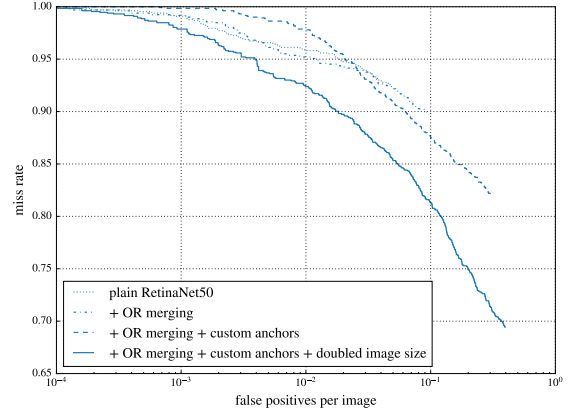


Figure 12: Performance on the total **field_test** showing the gradual improvements when adding our modifications to the plain RetinaNet50 variants, as described in Sec. 3.2.

Individual Human Detection A final evaluation investigates how well the pipeline detects human individuals: Every human in our novel dataset is labeled with a unique ID. Re-detections of the same individual can therefore be conveniently recognized. For search and rescue scenarios, one person does not necessarily need to be detected in every single frame. Instead, it is more important that an individual is detected at least once during the mission. It is therefore informative to investigate how many of all the distinct individual human IDs are detected by the pipeline as illustrated in Fig. 13 and 14. By calculating the miss-rate of actual human IDs instead of single ground-truth bounding boxes, these final results show final human ID miss-rates of the best performing RetinaNet50 of less than 30% while still making less than one false positive per image. This is a successful detection of over 70% of all individual humans at least once.

Qualitative samples Fig. 16 presents qualitative examples, including an example for the merging of the optical and infrared image and detected humans during a night flight.

7 Conclusion

This work presented our human detection framework that is able to detect, track, localize, and re-identify humans from UAVs with the help of an infrared and optical camera. Based on a detailed evaluation, it can be concluded that the RetinaNet variants, in particular RetinaNet50, are superior to YOLOv3 and to a classical human detection pipeline that served as a lower baseline. The major advantage of the RetinaNet architecture appears to be the focal loss that is capable of coping with drastic imbalances between the number of foreground and background samples. Moreover, customizing the anchors is crucial for the detection of humans seen from high altitudes. Enlarged or higher resolution images further improve the detection performance. Finally, the evaluation demonstrated that the logical OR merging scenario of both optical and thermal images helps to improve detection performance, especially for more challenging datasets like the introduced **field_test** sets. Both the quantitative and the qualitative evaluation emphasize the conclusion that our novel pipeline indeed also works on a challenging real-world dataset successfully exploiting and combining information from both optical and thermal images. Given the performance of detecting individual human IDs and the final qualitative examples, it could even be questioned whether the human detection performance might already be surpassed by RetinaNet50 under certain circumstances.

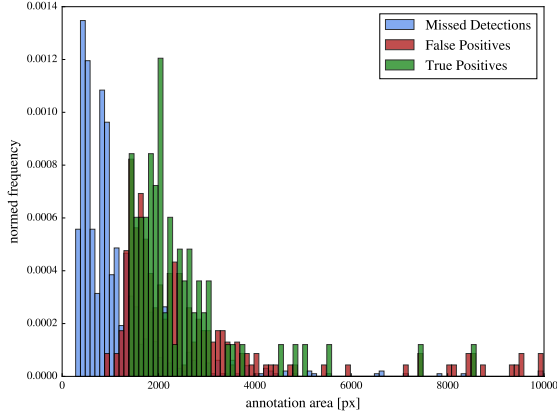


Figure 13: Bounding box size analysis of the best performing RetinaNet50 on the optical part of the **davos_rega** test sets. RetinaNet is able to generate true positives at a bounding box size of around 2000 px and fails to make any predictions with sizes below approximately 1500 px.

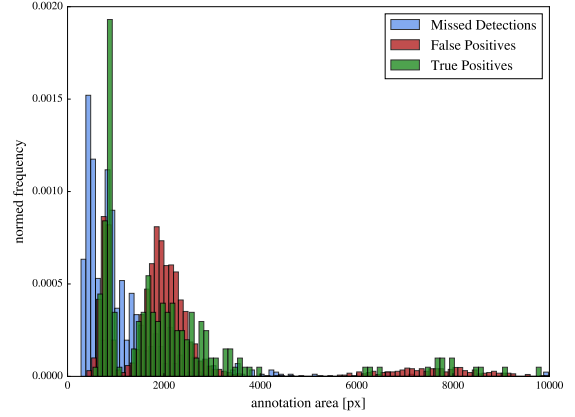


Figure 14: Bounding box size analysis of the best performing RetinaNet50 on the optical part of the **davos_rega** test sets using custom anchors. RetinaNet now generates most of its true positive predictions at a bounding box size of around 1000 px and is further able to make predictions across a wider range of sizes.

Acknowledgments

The research leading to these results has received funding from the Swiss air rescue organization [1]. Furthermore, the authors wish to thank the following persons for their help: Thomas Mantel (Sensor triggering and calibration), Yves Allenspach (camera mounts), and Daniel Hentzen (circular calibration target for thermal camera and graphical user interface).

Appendix

Table 5: Recorded and labeled internal datasets.

(a) Internal optical image sequences.

Sequence	Frames		Annotations				
	total	annotated	total	upright	sitting	lying	occluded
roof_new	1 900	1 815	4 748	4 748	0	0	584
roof_old	2 898	2 758	23 165	23 165	0	0	2 396
roof_test	447	447	1 462	1 462	0	0	172
roof_val	231	231	991	991	0	0	258
davos_rega_01	2 553	86	159	116	12	31	21
davos_rega_02	4 806	360	543	374	0	169	37
davos_rega_03	5 853	35	66	31	18	17	20
davos_rega_04	2 962	203	322	166	3	153	29
hinwil_01	2 069	210	417	417	0	0	59
hinwil_02	9 028	1 221	1 994	1 360	530	104	262
solair	7 698	97	155	121	0	34	38
Total	40 445	7 463	34 022	32 951	563	508	3 876

(b) Internal infrared image sequences.

Sequence	Frames		Annotations				
	total	annotated	total	upright	sitting	lying	occluded
roof_new	1 834	1 701	5 752	5 752	0	0	1 825
roof_old	1 480	1 316	6 141	6 141	0	0	477
roof_test	447	447	1 421	1 421	0	0	205
roof_val	231	231	627	627	0	0	138
davos_old	2 204	664	1 004	1 004	0	0	53
davos_rega_01	2 585	11	14	7	0	7	2
davos_rega_02	4 842	66	71	71	0	0	4
davos_rega_03	5 920	16	16	0	16	0	0
davos_rega_04	2 996	115	144	52	0	92	21
hinwil_01	2 012	114	194	194	0	0	17
hinwil_02	730	15	15	0	15	0	2
rothenturm	37 413	9 852	21 785	21 785	0	0	1 120
solair	27 324	0	0	0	0	0	0
tessin	1 011	43	44	27	0	17	1
Total	91 029	14 591	37 228	37 081	31	116	3 856

Table 6: All external datasets used for training

(a) Utilized external optical image sequences.

Sequence	Frames		Annotations	
	total	annotated	total	occluded
Mini-drone [9]				
set10 ^a	543	542	1 207	0
set13 ^b	570	569	569	0
Stanford drone [50]				
bookstore00	13 335	13 335	246 158	1 494
bookstore06	14 558	14 305	64 944	7 090
coupa01	11 966	11 966	71 136	3 726
coupa02	11 966	11 474	66 867	3 082
gates07	2 202	2 202	14 982	365
hyang02	12 272	12 272	172 880	4 855
hyang05	10 648	10 648	123 521	123
hyang07	574	574	14 637	221
hyang09	574	574	1 930	592
hyang10	9 928	9 928	64 228	7 845
hyang12	9 928	9 619	39 030	2 810
little00	1 518	1 518	24 517	508
little01	14 070	13 828	52 399	477
quad03	509	509	2448	0
UAV123 [38]				
bike01	553	553	553	0
person01	799	799	799	0
person02	2 514	2 514	2 514	0
person03	643	643	643	0
person04	254	254	254	0
person05	2 101	2 101	2 101	0
person06	658	658	658	0
person07	1 943	1 873	1 873	0
person08	126	126	126	0
person10	582	514	514	0
person12	1 621	1 548	1 548	0
person13	155	155	155	0
person14	2 034	2 034	2 034	0
person15	712	712	712	0
person16	1 147	1 038	1 038	0
person17	1 852	1 820	1 820	0
person22	24	24	24	0
person23	153	153	153	0
wakeboard02	733	733	733	0
wakeboard03	748	748	748	0
wakeboard04	586	586	586	0
wakeboard05	758	758	758	0
wakeboard06	401	401	401	0
wakeboard07	59	59	59	0
wakeboard08	321	321	321	0
41	136 638	134 988	982 578	33 188

^aOriginal name:

Normal_Static_Night_Empty_1_3_1 (test)

^bOriginal name:

Normal_Static_Day_Half_0_1_1 (training)

(b) Utilized external infrared image sequences.

Sequence	Frames		Annotations	
	total	annotated	total	occluded
ETH TIR [41]				
asl	659	659	1 021	191
sempach06	600	413	413	0
sempach07	370	359	1 391	140
sempach08	634	634	1 359	233
sempach09	576	576	982	59
sempach10	261	215	321	19
sempach11	197	192	707	113
sempach12	775	724	724	50
OTCVBS 1 [14]				
set01	31	31	91	0
set02	28	28	100	0
set03	23	23	101	0
set04	18	18	109	0
set05	23	23	101	0
set06	18	18	97	0
set07	22	22	94	0
set08	24	24	99	0
set09	73	73	95	0
set10	24	24	97	0
OTCVBS 11 [63]				
set02 ^a	1 273	1 273	69 841	0
set03 ^b	1 131	1 131	72 686	0
PTB TIR [34]				
stranger01	95	95	95	0
stranger02	280	280	280	0
stranger03	100	100	100	0
walking	315	315	315	0
VOT TIR [27]				
jacket	1 451	1 451	1 451	178
25	9 001	8 701	152 670	983

^aOriginal name: set2/seq3/nuc.^bOriginal name: set2/set4/nuc.

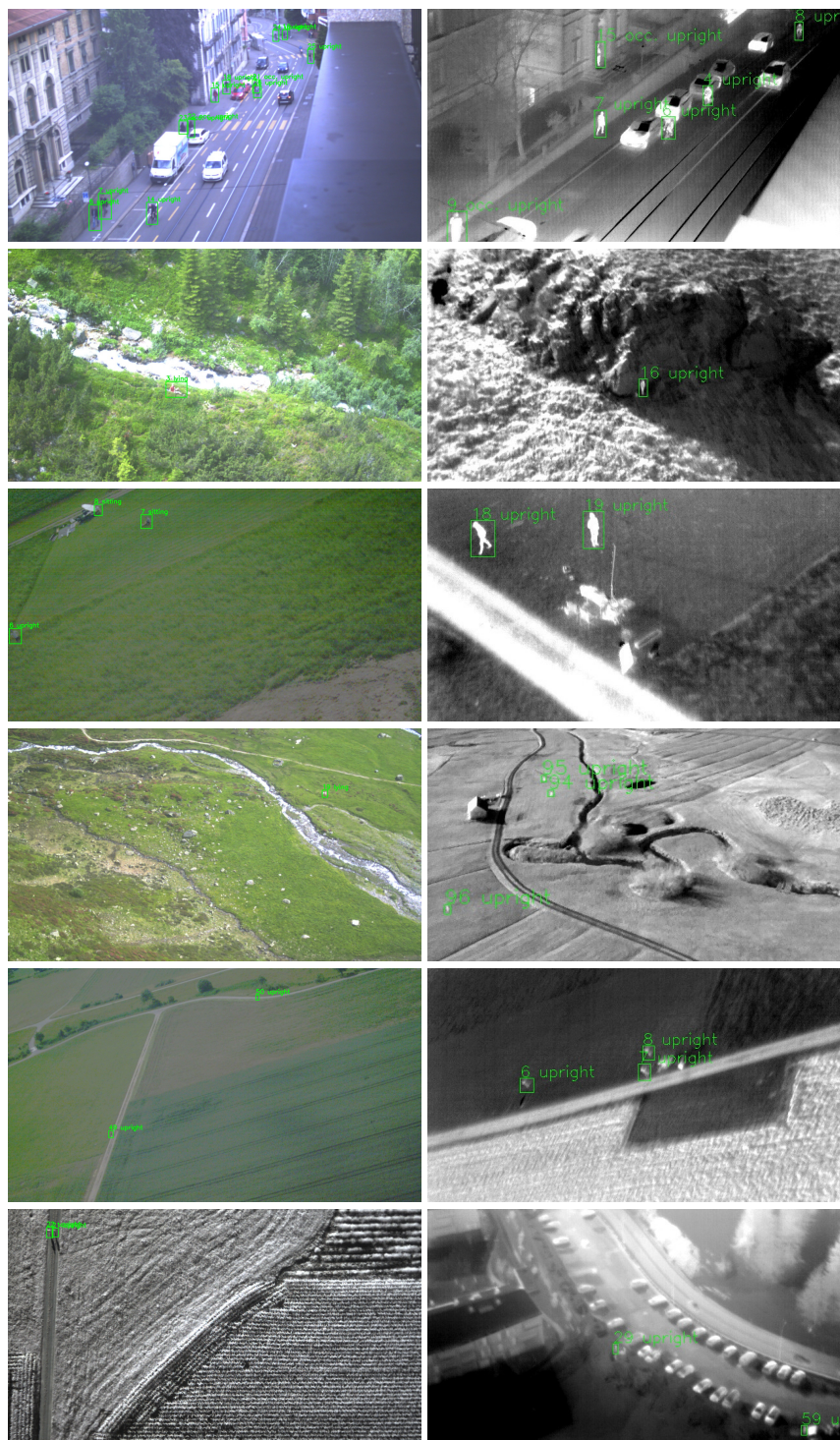


Figure 15: Annotated frames of the collected datasets containing a total of over 70 000 humans in different poses, in both optical and thermal imagery, and in a variety of different environments.

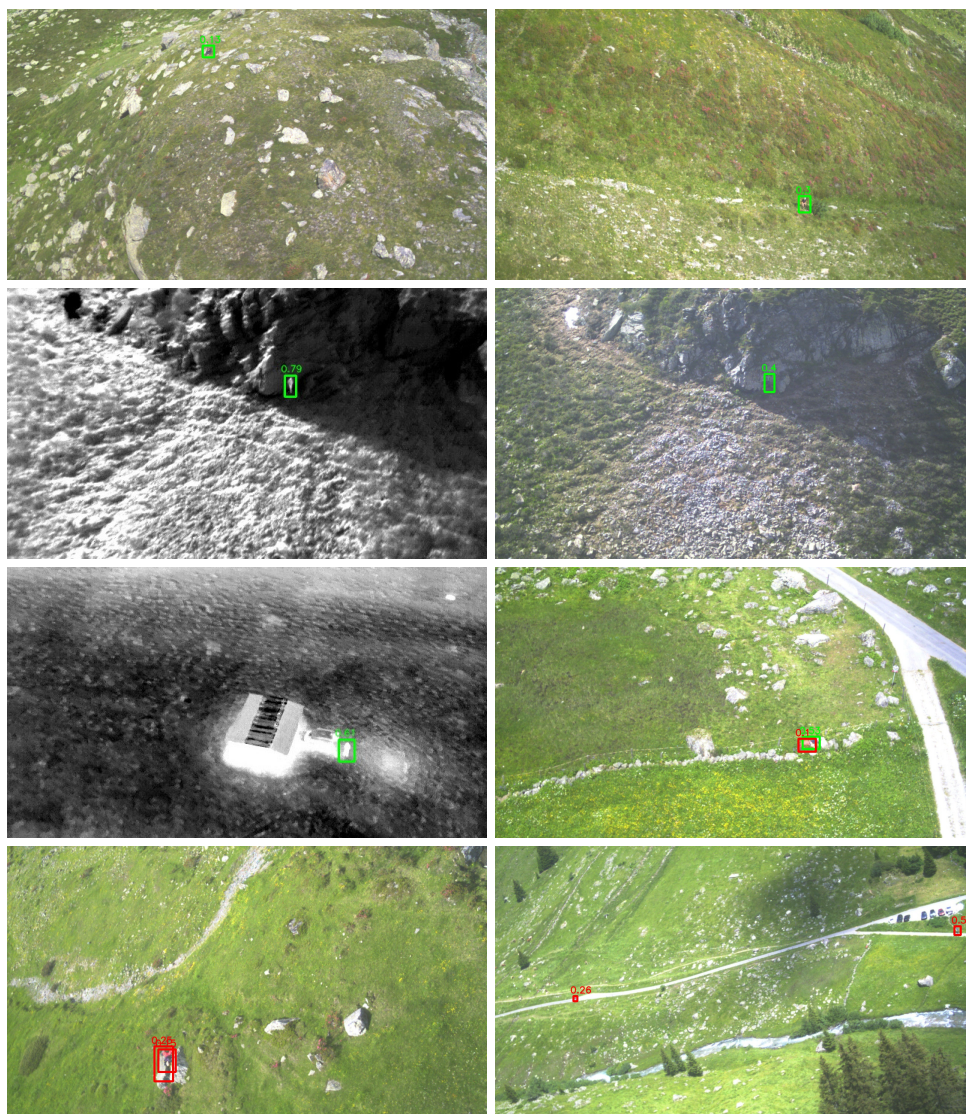


Figure 16: Qualitative samples. First row: Successfully detected humans, sitting and occluded. Second row: Working merging of optical and infrared image. Here, the human is easier to detect in the infrared spectrum. Third row: Night flight and detected mannequin that was placed before the flight. Fourth row: Correct detections by the network that have been missed during the manual labeling process.

References

- [1] Rega – the swiss air-rescue organization. www.rega.ch/en/. Accessed: 2020-08-02.
- [2] M. Andriluka, P. Schnitzspan, J. Meyer, et al. Vision Based Victim Detection from Unmanned Aerial Vehicles. In *International Conf. on Intelligent Robots and Systems (IROS), 2010 IEEE/RSJ*, pages 1740–1747. IEEE, 2010. ISBN 9781424466757. doi: 10.1109/IROS.2010.5649223.
- [3] B. Babenko, M. Yang, and S. Belongie. Visual tracking with online multiple instance learning. In *2009 IEEE Conference on Computer Vision and Pattern Recognition*, pages 983–990, 2009.
- [4] M. B. Bejiga, A. Zeggada, A. Nouffidj, and F. Melgani. A Convolutional Neural Network Approach for Assisting Avalanche Search and Rescue Operations with UAV Imagery. *Remote Sensing*, 9(2):100, 2017. ISSN 20724292. doi: 10.3390/rs9020100.
- [5] A. Bhattacharyya. On a measure of divergence between two statistical populations defined by their probability distributions. *Bull. Calcutta Math. Soc.*, 35:99–109, 1943.
- [6] P. Blondel, A. Potelle, C. Pegard, and R. Lozano. Human Detection in Uncluttered Environments: from Ground to UAV View. In IEEE, editor, *13th Int. Conf. on Control Automation Robotics & Vision (ICARCV), 2014*, pages 76–81, 2014. ISBN 9781479951994. doi: 10.1109/ICARCV.2014.7064283.
- [7] P. Blondel, A. Potelle, C. Pegard, and R. Lozano. Fast and viewpoint robust human detection for SAR operations. In *International Symposium on Safety, Security, and Rescue Robotics (SSRR), 2014 IEEE*, pages 1–6. IEEE, 2014. ISBN 9781479961399. doi: 10.1109/SSRR.2014.7017675.
- [8] E. Bondi, F. Fang, M. Hamilton, et al. SPOT Poachers in Action: Augmenting Conservation Drones With Automatic Detection in Near Real Time. *The Thirtieth AAAI Conference on Innovative Applications of Artificial Intelligence (IAAI-18)*, pages 7741–7746, 2018. URL <https://www.aaai.org/ocs/index.php/AAAI/AAAI18/paper/view/16282>.
- [9] M. Bonetto, P. Korshunov, G. Ramponi, and T. Ebrahimi. Privacy in Mini-drone Based Video Surveillance. *Proceedings - International Conference on Image Processing, ICIP*, 2015-Decem:2464–2469, 2015. ISSN 15224880. doi: 10.1109/ICIP.2015.7351245.
- [10] G. Bradski. The OpenCV Library. *Dr. Dobb’s Journal of Software Tools*, 2000.
- [11] G. Bradski. The OpenCV Library. *Dr. Dobb’s Journal: Software Tools for the Professional Programmer*, 25(11):120–123, 2000.
- [12] Y. C. Chang, H. T. Chen, J. H. Chuang, and I. C. Liao. Pedestrian Detection in Aerial Images Using Vanishing Point Transformation and Deep Learning. *2018 25th IEEE International Conference on Image Processing (ICIP)*, pages 1917–1921, 2018. ISSN 15224880. doi: 10.1109/ICIP.2018.8451144.
- [13] N. Dalal and W. Triggs. Histograms of Oriented Gradients for Human Detection. In *IEEE Computer Society Conference on Computer Vision and Pattern Recognition, 2005. CVPR 2005.*, volume 1, pages 886–893. Elsevier, 2005. ISBN 0-7695-2372-2. doi: 10.1109/CVPR.2005.177. URL <http://eprints.pascal-network.org/archive/00000802/>.
- [14] J. W. Davis and M. A. Keck. A Two-Stage Template Approach to Person Detection in Thermal Imagery. In *Workshops on Application of Computer Vision, 2005 IEEE*, pages 364–369. IEEE, 2005.
- [15] D. C. De Oliveira and M. A. Wehrmeister. Towards Real-Time People Recognition on Aerial Imagery Using Convolutional Neural Networks. In *19th Int. Symp. on Real-Time Distributed Computing (ISORC), 2016 IEEE*, pages 27–34. IEEE, 2016. ISBN 978-1-4673-9032-3. doi: 10.1109/ISORC.2016.14. URL <http://ieeexplore.ieee.org/document/7515608/>.
- [16] P. Dollár, C. Wojek, B. Schiele, and P. Perona. Pedestrian Detection: A Benchmark. *2009 IEEE Computer Society Conf. on Computer Vision and Pattern Recognition Workshops, CVPR Workshops 2009*, pages 304–311, 2009. ISSN 1063-6919. doi: 10.1109/CVPRW.2009.5206631.
- [17] P. F. Felzenszwalb, I. C. Society, R. B. Girshick, S. Member, D. Mcallester, and D. Ramanan. Object Detection with Discriminatively Trained Part-Based Models. *IEEE transactions on pattern analysis and machine intelligence*, 32(9):1627–1645, 2010. ISSN 0162-8828.

- [18] A. Filippov and O. Dzhimiev. Long range 3d with quadocular thermal (lwir) camera. *arXiv preprint arXiv:1911.06975*, 2019.
- [19] H. Flynn and S. Cameron. Multi-modal People Detection from Aerial Video. In *Proceedings of the 8th International Conference on Computer Recognition Systems CORES 2013*, pages 815–824. Springer, 2013. ISBN 9783319009698. doi: 10.1007/978-3-319-00969-8.
- [20] A. Gąszczak, T. P. Breckon, and J. Han. Real-time People and Vehicle Detection from UAV Imagery. In *Intelligent Robots and Computer Vision XXVIII: Algorithms and Techniques*, volume 7878, page 78780B. International Society for Optics and Photonics, 2011.
- [21] R. Girshick. Fast R-CNN. *CoRR*, pages 1440–1448, 2015.
- [22] R. Girshick, J. Donahue, T. Darrell, U. C. Berkeley, and J. Malik. Rich feature hierarchies for accurate object detection and semantic segmentation. *Proceedings of the IEEE conference on computer vision and pattern recognition*, pages 2–9, 2014.
- [23] D. Held, S. Thrun, and S. Savarese. Learning to track at 100 fps with deep regression networks. In *European Conference on Computer Vision*, pages 749–765. Springer, 2016.
- [24] J. F. Henriques, R. Caseiro, P. Martins, and J. Batista. Exploiting the circulant structure of tracking-by-detection with kernels. In *European conference on computer vision*, pages 702–715. Springer, 2012.
- [25] C. Herrmann, T. Müller, D. Willersinn, and J. Beyerer. Real-time person detection in low- resolution thermal infrared imagery with MSER and CNNs. In *Electro-Optical and Infrared Systems: Technology and Applications XIII*, volume 9987, page 99870I. Int. Society for Optics and Photonics, 2016. doi: 10.1117/12.2240940.
- [26] P. Kozierski, M. Lis, and J. Ziętkiewicz. Resampling in particle filtering-comparison. 2013.
- [27] M. Kristan, J. Matas, A. Leonardis, et al. A novel performance evaluation methodology for single-target trackers. *IEEE Transactions on Pattern Analysis and Machine Intelligence*, 38(11):2137–2155, Nov 2016. ISSN 0162-8828. doi: 10.1109/TPAMI.2016.2516982.
- [28] A. Krizhevsky and G. E. Hinton. ImageNet Classification with Deep Convolutional Neural Networks. In *Advances in neural information processing systems*, pages 1097–1105, 2012.
- [29] J. Kümmerle, T. Hinzmann, A. S. Vempati, and R. Siegwart. Real-Time Detection and Tracking of Multiple Humans from High Bird’s-Eye Views in the Visual and Infrared Spectrum. In *International Symposium on Visual Computing*, pages 545–556, 2016.
- [30] D. R. Lide. *CRC handbook of chemistry and physics*, volume 85. CRC press, 2004.
- [31] T.-Y. Lin, M. Maire, S. Belongie, et al. Microsoft COCO: Common Objects in Context. In *European conference on computer vision*, pages 740–755, 2014.
- [32] T.-y. Lin, P. Doll, R. Girshick, K. He, B. Hariharan, S. Belongie, F. Ai, and C. Tech. Feature Pyramid Networks for Object Detection. *Cvpr*, 1(2):3, 2017. ISSN 0006-291X. doi: 10.1109/CVPR.2017.106.
- [33] T. Y. Lin, P. Goyal, R. Girshick, K. He, and P. Dollar. Focal Loss for Dense Object Detection. *Proceedings of the IEEE International Conference on Computer Vision*, 2017-Octob:2999–3007, 2017. ISSN 15505499. doi: 10.1109/ICCV.2017.324.
- [34] Q. Liu and Z. He. PTB-TIR: A Thermal Infrared Pedestrian Tracking Benchmark. *arXiv preprint arXiv:1801.05944*, pages 1–10, 2018. URL <http://arxiv.org/abs/1801.05944>.
- [35] T. Liu, H. Y. Fu, Q. Wen, D. K. Zhang, and L. F. Li. Extended Faster R-CNN For Long Distance Human Detection: Finding Pedestrians in UAV Images. *2018 IEEE International Conference on Consumer Electronics, ICCE 2018*, pages 1–2, 2018. doi: 10.1109/ICCE.2018.8326306.
- [36] W. Liu, D. Anguelov, D. Erhan, C. Szegedy, S. Reed, C.-Y. Fu, and A. C. Berg. SSD : Single Shot MultiBox Detector. In *European Conf. on computer vision*, volume 1, pages 21–37. Springer, 2016. ISBN 9783319464480. doi: 10.1007/978-3-319-46448-0.
- [37] A. Lukezic, T. Vojir, L. ĚČCehovin Zajc, J. Matas, and M. Kristan. Discriminative correlation filter with channel and spatial reliability. In *Proceedings of the IEEE Conference on Computer Vision and Pattern Recognition*, pages 6309–6318, 2017.

- [38] M. Mueller, N. Smith, and B. Ghanem. A Benchmark and Simulator for UAV Tracking. In *Proc. of the European Conf. on Computer Vision (ECCV)*, pages 445–461. Springer, 2016.
- [39] D. T. Nguyen, W. Li, and P. O. Ogunbona. Human detection from images and videos: A survey. *Pattern Recognition*, 51:148–175, 2016. ISSN 00313203. doi: 10.1016/j.patcog.2015.08.027. URL <http://dx.doi.org/10.1016/j.patcog.2015.08.027>.
- [40] A. G. Perera, A. Al-Naji, Y. W. Law, and J. Chahl. Human Detection and Motion Analysis from a Quadrotor UAV. In *IOP Conf. Series: Materials Science and Engineering*, volume 405, page 12003. IOP Publishing, 2018. doi: 10.1088/1757-899X/405/1/012003.
- [41] J. Portmann, S. Lynen, M. Chli, and R. Siegwart. People Detection and Tracking from Aerial Thermal Views. In *International Conf. on Robotics and Automation (ICRA), 2014 IEEE*, pages 1794–1800. IEEE, 2014. ISBN 9781479936854.
- [42] S. Prakash, P. Y. Lee, and T. Caelli. 3d mapping of surface temperature using thermal stereo. In *2006 9th International Conference on Control, Automation, Robotics and Vision*, pages 1–4, Dec 2006. doi: 10.1109/ICARCV.2006.345342.
- [43] M. Quigley, B. Gerkey, K. Conley, J. Faust, T. Foote, J. Leibs, E. Berger, R. Wheeler, and A. Ng. Ros: an open-source robot operating system. In *Proc. of the IEEE Intl. Conf. on Robotics and Automation (ICRA) Workshop on Open Source Robotics*, Kobe, Japan, May 2009.
- [44] J. Rangel, S. Soldan, and A. Kroll. 3d thermal imaging: Fusion of thermography and depth cameras. In *International Conference on Quantitative InfraRed Thermography*, 2014.
- [45] J. Redmon and A. Farhadi. YOLO9000: Better, faster, stronger. *Proceedings - 30th IEEE Conf. on Computer Vision and Pattern Recognition, CVPR 2017*, 2017-January:6517–6525, 2017. ISSN 0146-4833. doi: 10.1109/CVPR.2017.690.
- [46] J. Redmon and A. Farhadi. YOLOv3: An Incremental Improvement. *arXiv preprint arXiv:1804.02767*, 2018. ISSN 0146-4833. doi: 10.1109/CVPR.2017.690. URL <http://arxiv.org/abs/1804.02767>.
- [47] J. Redmon, S. Divvala, R. Girshick, and A. Farhadi. You Only Look Once: Unified, Real-Time Object Detection. In *Proceedings of the IEEE Conf. on computer vision and pattern recognition*, pages 779–788, 2016. ISBN 978-1-4673-8851-1. doi: 10.1109/CVPR.2016.91. URL <http://arxiv.org/abs/1506.02640>.
- [48] J. Rehder, K. Gupta, S. Nuske, and S. Singh. Global pose estimation with limited gps and long range visual odometry. In *2012 IEEE international conference on robotics and automation*, pages 627–633. IEEE, 2012.
- [49] S. Ren, K. He, R. Girshick, and J. Sun. Faster R-CNN: Towards Real-Time Object Detection with Region Proposal Networks. In *Advances in neural information processing systems*, pages 91–99, 2015.
- [50] A. Robicquet, A. Sadeghian, A. Alahi, and S. Savarese. Learning social etiquette: Human trajectory understanding in crowded scenes. *Lecture Notes in Computer Science*, 9912 LNCS:549–565, 2016. ISSN 16113349. doi: 10.1007/978-3-319-46484-8_33.
- [51] C. Rother, V. Kolmogorov, and A. Blake. " grabcut" interactive foreground extraction using iterated graph cuts. *ACM transactions on graphics (TOG)*, 23(3):309–314, 2004.
- [52] P. Rudol and P. Doherty. Human Body Detection and Geolocalization for UAV Search and Rescue Missions Using Color and Thermal Imagery. In *Aerospace Conf., 2008 IEEE*, pages 1–8. IEEE, 2008. ISBN 1424414881. doi: 10.1109/AERO.2008.4526559.
- [53] O. Russakovsky, J. Deng, H. Su, et al. ImageNet Large Scale Visual Recognition Challenge. In *Int. J. of Computer Vision*, volume 115, pages 211–252. Springer US, 2015. ISBN 0920-5691. doi: 10.1007/s11263-015-0816-y. URL <http://dx.doi.org/10.1007/s11263-015-0816-y>.
- [54] P. Saponaro, S. Sorensen, S. Rhein, and C. Kambhamettu. Improving calibration of thermal stereo cameras using heated calibration board. In *2015 IEEE International Conference on Image Processing (ICIP)*, pages 4718–4722, Sep. 2015. doi: 10.1109/ICIP.2015.7351702.

- [55] A. Sathyan, J. Cohen, and M. Kumar. Deep Convolutional Neural Network For Human Detection And Tracking In FLIR Videos. In *AIAA Infotech @ Aerospace*, page 1412. American Institute of Aeronautics and Astronautics, 2016. ISBN 978-1-62410-388-9. doi: 10.2514/6.2016-1412. URL <http://arc.aiaa.org/doi/10.2514/6.2016-1412>.
- [56] D. Simon. *Optimal state estimation: Kalman, H infinity, and nonlinear approaches*. John Wiley & Sons, 2006.
- [57] K. Simonyan and A. Zisserman. Very Deep Convolutional Networks for Large-Scale Image Recognition. *arXiv preprint arXiv:1409.1556*, pages 1–14, 2014. ISSN 09505849. doi: 10.1016/j.infsof.2008.09.005. URL <http://arxiv.org/abs/1409.1556>.
- [58] K. Skala, T. Lipić, I. Sović, L. Gjenero, and I. Grubišić. 4d thermal imaging system for medical applications. *Periodicum biologorum*, 113(4):407–416, 2011.
- [59] A. S. Vempati, G. Agamennoni, T. Stastny, and R. Siegwart. Victim Detection from a Fixed-Wing UAV: Experimental Results. In *Advances in Visual Computing*, pages 432–443. Springer, 2015.
- [60] S. Vidas, R. Lakemond, S. Denman, C. Fookes, S. Sridharan, and T. Wark. A mask-based approach for the geometric calibration of thermal-infrared cameras. *IEEE Transactions on Instrumentation and Measurement*, 61(6):1625–1635, June 2012. ISSN 1557-9662. doi: 10.1109/TIM.2012.2182851.
- [61] P. Viola and M. Jones. Rapid Object Detection using a Boosted Cascade of Simple Features. In *Proceedings of the 2001 IEEE Computer Society Conf. on Computer Vision and Pattern Recognition, 2001. CVPR 2001.*, volume 1. IEEE, 2001. ISBN 0769512720.
- [62] X. Wang, P. Cheng, X. Liu, and B. Uzochukwu. Fast and Accurate, Convolutional Neural Network Based Approach for Object Detection from UAV. *arXiv preprint arXiv:1808.05756*, 2018. URL <http://arxiv.org/abs/1808.05756>.
- [63] Z. Wu, N. Fuller, D. Theriault, and M. Betke. A Thermal Infrared Video Benchmark for Visual Analysis. *IEEE Computer Society Conf. on Computer Vision and Pattern Recognition Workshops*, pages 201–208, 2014. ISSN 21607516. doi: 10.1109/CVPRW.2014.39.
- [64] Z. Yu, S. Lincheng, Z. Dianle, Z. Daibing, and Y. Chengping. Camera calibration of thermal-infrared stereo vision system. In *2013 Fourth International Conference on Intelligent Systems Design and Engineering Applications*, pages 197–201. IEEE, 2013.
- [65] K. Yun, L. Nguyen, T. Nguyen, et al. Small target detection for search and rescue operations using distributed deep learning and synthetic data generation. *CoRR*, abs/1904.11619, 2019. URL <http://arxiv.org/abs/1904.11619>.